Vacuum 113 (2015) 52–58

Contents lists available at ScienceDirect

Vacuum

journal homepage: www.elsevier.com/locate/vacuum

Structural and XPS characterization of ALD Al_2O_3 coated porous silicon

Igor Iatsunskyi [a, b, *], Mateusz Kempiński [a, c], Mariusz Jancelewicz [a], Karol Załęski [a], Stefan Jurga [a], Valentyn Smyntyna [b]

[a] NanoBioMedical Center, Adam Mickiewicz University, ul.Umultowska, 85, 61-614, Poznan, Poland
[b] Department of Experimental Physics, Odessa I.I. Mechnikov National University, 42, Pastera Str., 65023, Odessa, Ukraine
[c] Faculty of Physics, Adam Mickiewicz University, Umultowska 85, 61-614, Poznan, Poland

ARTICLE INFO

Article history:
Received 23 October 2014
Received in revised form
16 December 2014
Accepted 17 December 2014
Available online 24 December 2014

Keywords:
Atomic layer deposition
Aluminum oxide
Porous silicon
XPS

ABSTRACT

Al_2O_3 thin films were grown on highly-doped p-Si (100) macro- and mesoporous structures by atomic layer deposition (ALD) using trimethylaluminum (TMA) and water H_2O as precursors at 300 °C. The porous silicon (PSi) samples were fabricated utilizing a metal-assisted chemical etching process (MACE). The morphology of the deposited films and initial silicon nanostructures were investigated by means of scanning electron microscopy (SEM) with energy dispersive X-ray spectroscopy (EDX). X-ray photoelectron spectroscopy (XPS) was used to analyze the chemical elemental composition by observing the behavior of the Al 2p, O 1s and C 1s lines. Calculated Auger parameter and binding energy analysis confirmed Al_2O_3 formation. The measurement of band gap energies of Al_2O_3 was performed.

1. Introduction

Silicon nanostructures (e.g. porous silicon – PSi) have attracted extensive attention due to the unique structural and optoelectronic properties. Because of its unique physical properties, PSi has a large number of applications in optoelectronics [1,2], biotechnology [3,4], renewable energy [5,6] etc. The PSi structures also exhibit a great potential in optical sensor applications due to the possible tuning of refractive index useable for detection of biological substances or chemical vapors [5,6]. Besides, any device application of PSi is bound to be successful because of the low cost of silicon and compatibility with the modern integrated circuit (IC) industry.

However, optical, structural and sensing properties of the PSi are not very stable [7]. Therefore, the issue of the PSi stability is significant and requires further investigations. The surface passivation seems to be an effective way to stabilize the PSi properties and one of the possible materials for passivation is aluminum oxide (Al_2O_3).

Al_2O_3 ultra-thin films have been investigated for many applications like surface passivation [8,9], gas diffusion barrier [10], interfacial buffering for high-*k* dielectrics [11,12], and nanolaminates [13,14]. It is expected that Al_2O_3 coatings of PSi will form nanostructures possessing stable optical, structural and electrical properties that can be used for development of new more stable devices [15–21].

The increased surface area of PSi requires the ability to cover conformally the walls of a structure with the high aspect ratio. This is extremely challenging for most thin film deposition methods. It is well known that only atomic layer deposition (ALD) can uniformly coat each pore over the entire pore length [22–24]. Therefore, coating PSi with Al_2O_3 by ALD would be the ideal approach to realize the surface passivation.

In the present study, we show a comparison of the Al_2O_3 – PSi prepared on macro- and mesoporous structures based on scanning electron microscopy (SEM) and X-ray photoelectron spectroscopy (XPS) measurements. XPS measurements allowed us to estimate the band gap energy and calculate the stoichiometry of Al_2O_3, providing a new understanding of morphology and phase evolution during the ALD of the porous materials.

2. Materials and methods

2.1. Materials and porous silicon fabrication

Silicon wafers (<0.005 Ωcm resistivity, polished on the (100) face, B-doped) were obtained from SIEGERT WAFER GmbH. Other chemicals were purchased from Sigma–Aldrich Chemicals.

* Corresponding author. Department of Experimental Physics, Odessa I.I. Mechnikov National University, 42, Pastera Str., 65023, Odessa, Ukraine.
E-mail address: yatsunskiy@gmail.com (I. Iatsunskyi).

http://dx.doi.org/10.1016/j.vacuum.2014.12.015
0042-207X/

The porous silicon samples were fabricated utilizing a metal-assisted chemical etching process (MACE) [25]. Silicon samples (1 × 1 cm), after standard RCA cleaning, were cleaned with acetone, isopropanol and deionized water via ultrasonic cleaning. A thin oxide layer was formed, and the surface became hydrophilic. This oxide layer was removed by dipping the samples into a dilute HF (5%) solution. The silver particles, which act as catalysts to assist the etching of silicon, were deposited on Si samples by immersion in 0.2 M HF and 10^{-4} M $AgNO_3$ metallization aqueous solutions. The time of immersion was ranged from 30 s to 120 s. After the electroless metallization, two sets of samples were manufactured. The wafers were etched in aqueous solutions containing HF (40%), H_2O_2 (30%), and ultrapure H_2O at ratio concentration – 1) $H_2O_2/H_2O/HF = 80/80/20$ – samples №1 – S1; 2) $H_2O_2/H_2O/HF = 15/80/40$ – samples №2 – S2; for 60 min. After etching, the samples were etched in HNO_3 solution to remove silver particles. After that, samples were dipped into HF (5%) to remove oxide and then cleaned with deionized water and blown dry with nitrogen or argon. The etching and immersion procedures were performed at room temperature.

2.2. Atomic layer deposition of Al_2O_3 thin films

The samples of porous silicon were placed in the ALD reactor (Picosun). The Al_2O_3 thin films were deposited on the PSi substrates using trimethylaluminum (TMA) and water H_2O as ALD precursors. Nitrogen (N_2) served both as a carrier and a purging gas. TMA and H_2O were evaporated at 20 °C. In this study, the standard cycle consisted of 0.1 s exposure to TMA, 3 s N_2 purge, 0.1 s exposure to water and 4 s N_2 purge. The total flow rate of the N_2 was 150 sccm (standard cubic centimetres per minute). The Al_2O_3 thin films were grown at 300 °C. The growth rate per cycle (GPC) was typically 1 Å/cycle for Al_2O_3. It is well known, that Al_2O_3 ALD results in the formation of amorphous films in the temperature range of 200–500 °C and film thickness up to 200 nm [26]. According to that, the Al_2O_3 film prepared at the above conditions should definitely have the amorphous structure.

2.3. Characterization

Several analysis and characterization techniques were employed to investigate PSi and Al_2O_3 thin films. The surface morphology was investigated by scanning electron microscopy (JEOL, JSM-7001F) with the energy dispersive X-ray spectroscopy (EDX) analyzer. The cross-sections for SEM investigations were prepared by Focused Ion Beam (JEOL, JIB-4000). Surface structural properties of the PSi and ALD Al_2O_3 thin films were analyzed by means of XPS technique mounted within the Omicron Nanotechnology multiprobe UHV system, using a monochromatized Al-Kα X-ray as the excitation source and choosing C 1s (284.5 eV) as the reference line. XPS was conducted under ultrahigh vacuum (10^{-10} mbar). CasaXPS software was used to analyze the XPS data.

3. Results and discussion

3.1. Structural characterization (SEM and EDX)

Typical plan-view scanning electron microscope (SEM) images of PSi and PSi-Al_2O_3 are shown in Fig. 1. The morphology of the PSi

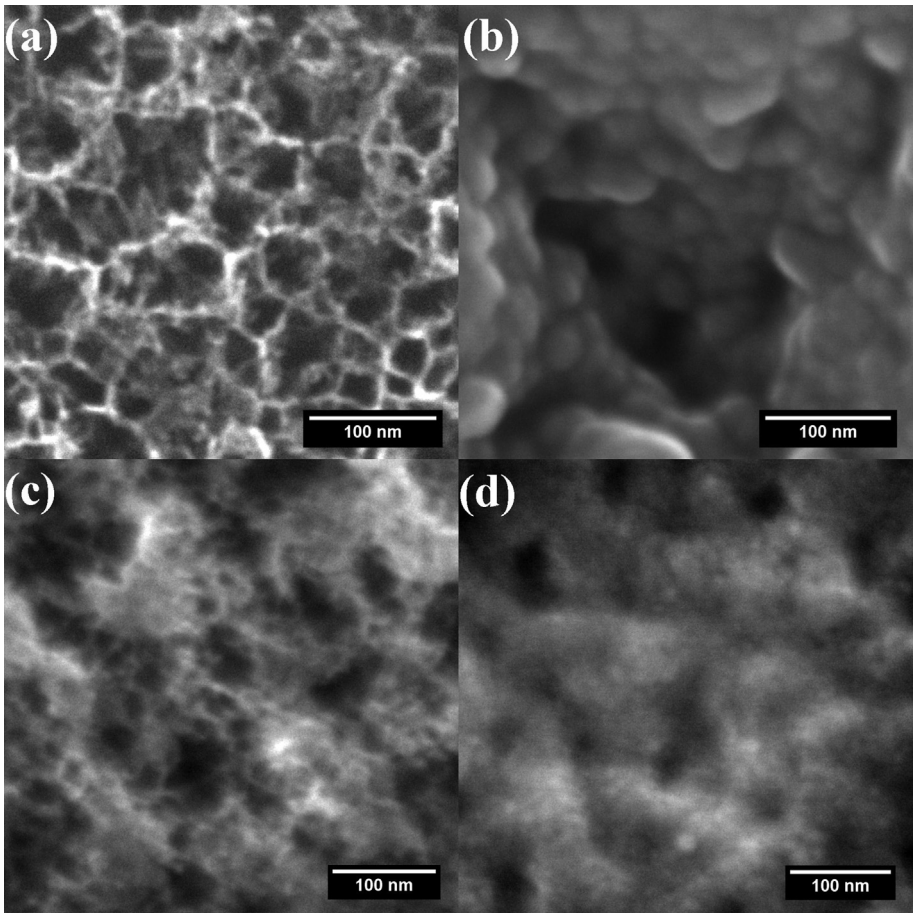

Fig. 1. (a) Macro-PSi surface, (b) macro-PSi surface after 150 ALD cycles, (c) meso-PSi surface, (d), meso-PSi surface after 150 ALD cycles.

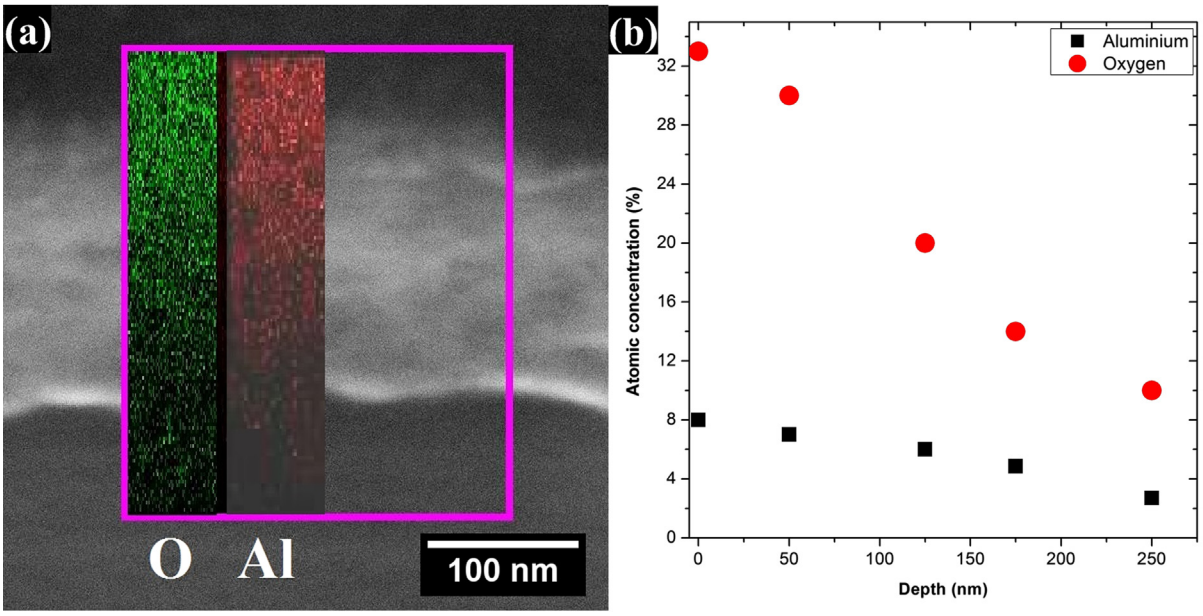

Fig. 2. (a) EDX elemental mapping of macro-PSi surface after 150 ALD cycles; (b) the concentration-depth profile of aluminum and oxygen for Al_2O_3-macro-PSi. Estimation was based on the SEM-EDX line scans of the sample cross-section prepared by FIB.

layer obtained by the MACE is quite different for sample 1 – S1 (Fig. 1a) and sample 2 – S2 (Fig. 1c). The PSi layer consists of a large number of small pores for S2 – mesoporous-Si (meso-PSi) structure (Fig. 1c), comparing to the S1, where one can see the macroporous Si (macro-PSi) structure (Fig. 1a). The macro-PSi layers exhibit the matt and dark surface, whereas the meso-PSi (Fig. 1c) films have a homogeneous interface and mirror-like surface. The mean pore size is less than 10 nm for meso-PSi (S2) and more than 50 nm for macro-PSi (S1). The cross-sectional SEM view of the same sample shows the presence of large pores propagating into the bulk from the surface in a perpendicular manner for S1 and in a random manner for S2.

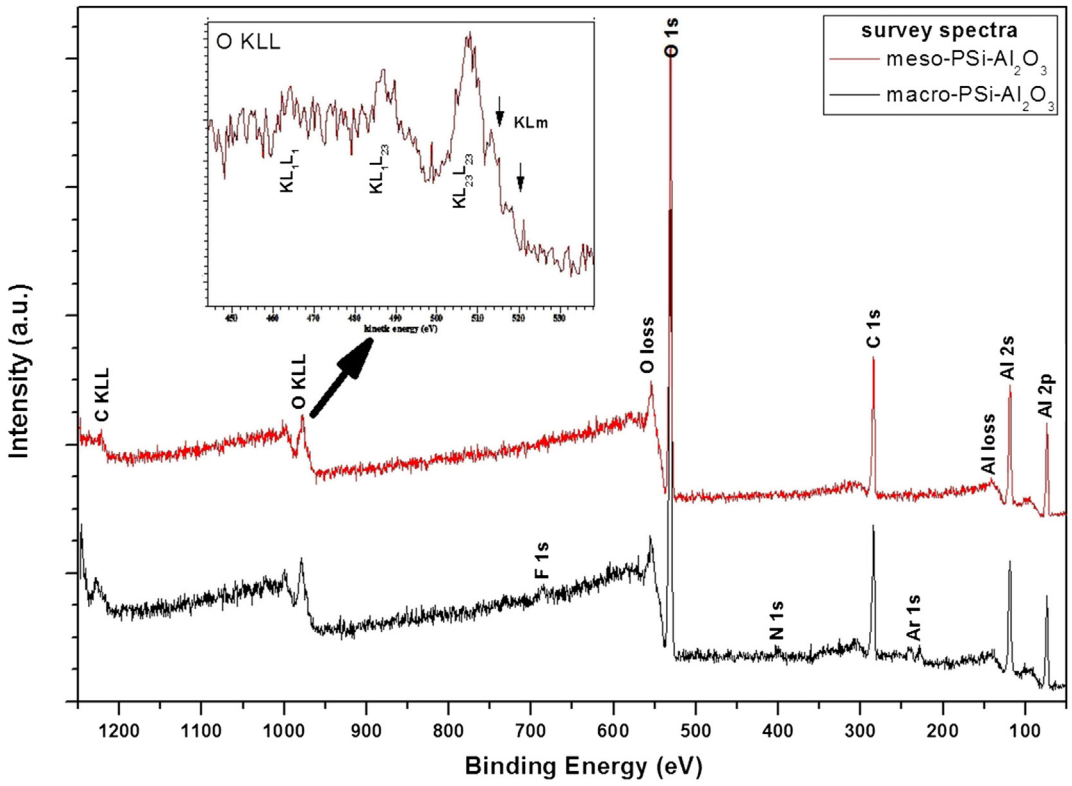

Fig. 3. XPS survey spectra of the meso-PSi-Al_2O_3 (red curve) and macro-PSi-Al_2O_3 (black). The main core levels are labeled. The data are normalized to each O1s peak maximum and separated vertically. (For interpretation of the references to colour in this figure legend, the reader is referred to the web version of this article.)

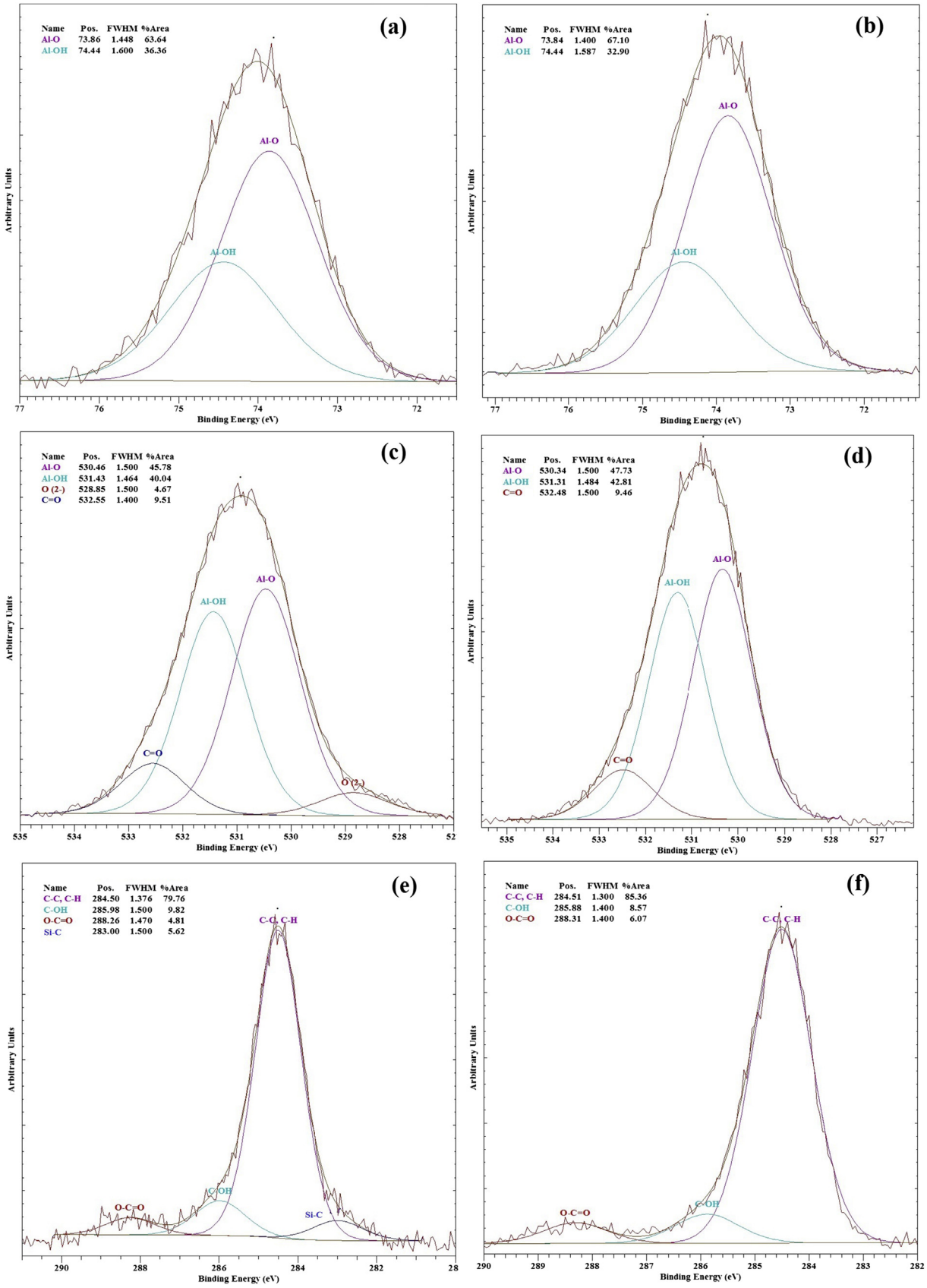

Fig. 4. High resolution XPS core level spectra: (a) Al 2p (c) O 1s (e) C 1s macro-PSi-Al_2O_3 and (b) Al 2p (d) O 1s (f) C 1s meso-PSi-Al_2O_3.

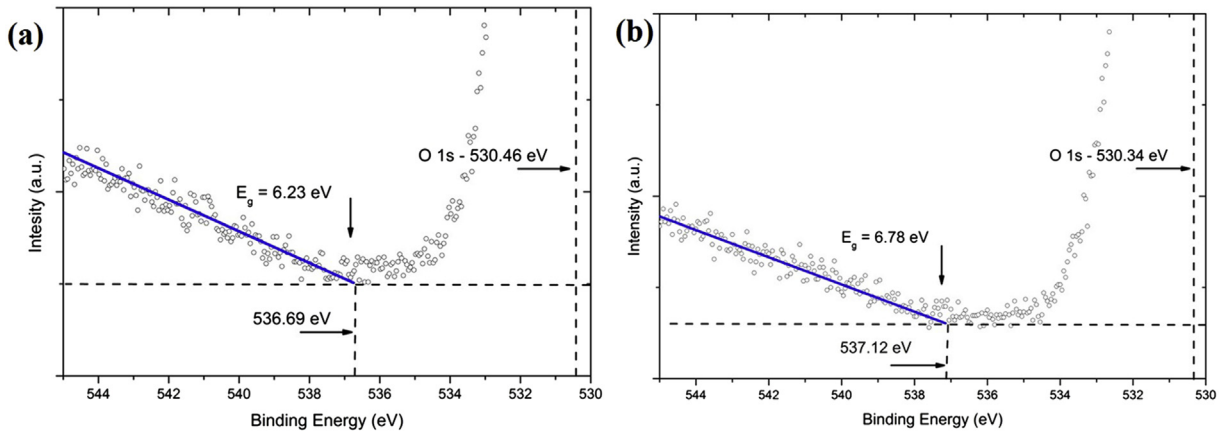

Fig. 5. The band gap of the (a) macro-PSi-Al_2O_3 and (b) meso-PSi-Al_2O_3 from the O 1s peak obtained by high resolution XPS.

Cross-sectional SEM images indicate that the ALD Al_2O_3 layer infiltrates and conformally coats the pores of both samples. For meso-PSi surface (S2), the film consists of spherical grains uniformly distributed over the surface (Fig. 1d). For macro-PSi, the film has quite homogeneous structure on the surface and granular structure inside the pores (Fig. 1b). An average grain size of S1 ranged from 40 to 60 nm and from 6 to 10 nm for S2.

Based on obtained SEM results we can suggest a model of the ALD film growth inside the porous media. In the case of PSi, the layers of Al_2O_3 start to grow horizontally along the pore wall. Depending on the diameter of the pore, the layers of Al_2O_3 first go towards each other and then may fit closely. Taking into account the value of GPC = 1 Å/cycle, we can imagine the growth of ALD film inside the pore as a deposition of 1 Å layer per cycle. The inner diameter of the pore is reduced by 2 Å every ALD cycle. The pore having diameter 10 nm would be completely filled by Al_2O_3 after 50 ALD cycles. But, as the diameter becomes smaller, the diffusion of precursor molecules inside the pore decreases. And we should conclude that the minimum number of ALD cycles have to be higher than 50 cycles. In the case of mesoporous structure, when the pore diameter is less than 10 nm, the "closing" of the opposite Al_2O_3 layers starts approximately after 60–80 ALD cycles. After the "closing" of the opposite Al_2O_3 layers inside the pore, the film grows upwards alike a plane surface.

EDX measurements were carried out to evaluate the chemical composition of ALD Al_2O_3 films deposited on PSi and the distribution of the Al_2O_3 inside the porous structure. EDX confirms that the PSi contains Al, O and Si not only on the top of the film but also within the porous matrix (Fig. 2). The EDX mapping image showing the distribution of Al and O atoms is presented in Fig. 2(a). Fig. 2(b) shows the concentration-depth profile of aluminum and oxygen for the Al_2O_3-macro-PSi. The concentration of O and Al has a decreasing trend from top to bottom of the PSi layer. Calculated ratio of O/Al shows the excess of oxygen atoms. This is probably due to the different amounts of H_2O and TMA molecules diffused into PSi layer and the consumption of a small excess amount of H_2O for oxidation of PSi. It is well known that diffusivity is larger for molecules with smaller molecular weight, and therefore, more H_2O molecules should diffuse into the PSi than TMA. For the Al_2O_3-meso-PSi we obtained similar results but with smaller concentration of Al and O.

3.2. XPS analysis

3.2.1. Survey spectra

In order to determine the chemical composition of the Al_2O_3 – PSi XPS measurements were performed. The XPS survey spectrum is presented in Fig. 3. The XPS survey spectra of macro-PSi-Al_2O_3 represent mainly Al, O and C contributions but also F, N and Ar contaminations. In the meso-PSi-Al_2O_3 sample, one can notice only peaks corresponding to Al, O and C. The presence of fluorine, nitrogen and argon atoms in the macro-PSi-Al_2O_3 could be explained by contaminations during ALD and MACE processes. This indicates the high adsorption capability of the macro-PSi surface.

Survey spectra of PSi surfaces after 150 ALD cycles indicates appearance of many peaks at 74 eV, 118 eV, 285 eV, 531 eV, 975 eV and 1230 eV which represent the binding energies of Al 2p, Al 2s, C 1s, O 1s, O KLL and C KLL respectively (Fig. 3). There are also few peaks corresponding to the plasmon losses [27]. As can be seen in Fig. 4, the bulk plasmon loss peaks are observed at approximately 555 and 140 eV, corresponding to bulk plasmon energy $E_p = 555\ eV - E_{O\ 1s} = 23\ eV$ and $E_p = 140\ eV - E_{Al\ 2s} = 22\ eV$.

The main peak of the O (KLL) Auger series: O ($KL_{23}\ L_{23}$), occurs at kinetic energy of 507 eV (Fig. 3 inset) for both samples. One can notice peaks corresponding to a transition from the KL level of oxygen to the m level of aluminum. By using the values of O 1s binding energy and O ($KL_{23}\ L_{23}$) kinetic energy, we calculate the Auger parameter as defined by Wagner [28]. The Auger parameter is a good tool to determine the phase, the stoichiometry and the crystallinity of surfaces. Unfortunately, we could not reveal the Auger peak of Al. Therefore, we used the Auger parameter of oxygen. Our measurements lead to a value of 1039 eV which is in good agreement with the previous data collected for Al_2O_3 [29].

We calculated the elemental ratio of oxygen to aluminum (O/Al) atomic ratio for macro- and meso-PSi-Al_2O_3. The peak areas of the Al–O contributions within the O1s and Al2p core levels were used. The O/Al atomic ratios were calculated to be 1.69 and 1.58 for macro-PSi-Al_2O_3 and meso-PSi-Al_2O_3, respectively. Obtained values are close to the stoichiometric value of 1.5.

3.2.2. Al 2p, O 1s and C 1s core levels

The detailed spectra of the Al 2p, O 1s and C 1s core levels are shown in Fig. 4. The presence of Al–O bonds in the Al_2O_3 film is confirmed by the binding energies of the Al 2p peak at 74.1 ± 0.1 eV and Al 2s peak at 119.0 ± 0.1 eV for macro-PSi-Al_2O_3 and Al 2p peak at 74.0 ± 0.1 eV and Al 2s peak at 119.0 ± 0.1 eV for meso-PSi-Al_2O_3 [30–32].

For both samples, Al 2p peak could be fitted as two symmetric single peaks. The presence of Al–O and Al–OH bonds in the Al_2O_3 film is confirmed by the binding energies of the Al 2p peak at around 73.8 eV/74.4 eV for macro-/meso-PSi-Al_2O_3 [33]. The fact that the aluminum in the PSi is completely oxidized by the surface-saturation reaction during the ALD deposition could be confirmed

by the absence of Al–Al bonds around 73 eV [30]. Besides, the binding energy difference between Al 2p and O 1s was found to be 456.7 ± 0.1 eV for both samples. What is in a good agreement with the previously reported values [33].

The O 1s peak at 531.5 eV is relatively broad and asymmetric as it is associated with different types of bonds. Further deconvolution revealed four/three distinct components, the strongest peak locating at 530.4 ± 0.2 eV originated from Al–O bonds, the other peak 531.4 ± 0.2 eV associated with Al–O–H hydroxyl groups appeared due to H_2O in ALD [34,35]. The presence of Al–OH-type chemical defect in ALD films leading to excess of oxygen atoms mainly located near the interface. The peak at 528.8 ± 0.2 eV for the macro-PSi-Al_2O_3 is that due to adsorbed oxygen (Fig. 4c) [36]. This fact also confirms the higher adsorption capability of the macro-PSi-Al_2O_3 compared to the meso-PSi-Al_2O_3. The peak at 532.5 ± 0.2 eV could be related to carbon–oxygen radicals.

The deconvolution of the C 1s peaks was carried out. The deconvolution revealed three mail distinct components, the strongest peak locating at 284.5 ± 0.1 eV originated from C–C bonds. Other two peaks at approximately 286 ± 0.2 eV and 288 ± 0.2 eV are associated with C–O and COO bonds, respectively [37]. These reaction products might be identified as fragments of the precursor which do not desorb completely during the purging periods. Increasing of the purging time slightly reduces the concentration of carbon radicals but not desorb completely. We have also revealed the small peak at 283 ± 0.1 eV in the macro-PSi-Al_2O_3. Probably, this peak corresponds to Si–C bonds (Fig. 4e) [38]. EDX and SEM of the PSi surface confirm the increased concentration of carbon and formation of crystallites consisting of silicon, carbon, oxygen and silver atoms (not shown here). We can suggest that silver particles serve as a nucleation center for crystallites formation during MACE. However, the present explanation is tentative and requires further theoretical and experimental proof.

3.2.3. Band gap energy determination

It is well known, that the difference in energy between the elastic peak (e.g. oxygen peak -$E_{O\ 1s}$) and the onset of inelastic losses (E_{loss}) corresponds to the energy gap (E_g) [39]. In order to find the band gap energy, one should perform a linear fit to the measured loss spectra curve near the elastic peak and then to subtract the Shirley background fitting (the background "zero" level). The intersection of the linear-fit line and the background "zero" level gives us the onset of inelastic losses. Thus, the band gap energy is equal to the difference between the elastic peak energy and the onset of inelastic losses $E_g = E_{loss} - E_{O\ 1s}$.

To calculate the band gap we performed analysis of the O 1s peak (Fig. 5). The locations of the O 1s elastic peak were determined to be 530.46 eV (macro-PSi-Al_2O_3) and 530.34 eV (meso-PSi-Al_2O_3). The intersections of liner-fit line and the background "zero" level were calculated to occur at 536.69 eV and 537.12 eV for macro- and meso-PSi-Al_2O_3, respectively. We obtained $E_g = 6.2 \pm 0.1$ eV for the macro-PSi-Al_2O_3 and $E_g = 6.8 \pm 0.1$ eV for the meso-PSi-Al_2O_3. Our obtained value of about 6.5 eV is low compared to the band gap of 8.8 eV reported for amorphous Al_2O_3 [39]. This can be explained in terms of the highly defected structure of Al_2O_3 for both samples. But comparing the O/Al atomic ratio (1.69 vs. 1.58) and the band gap energy (6.2 eV vs. 6.8 eV) for macro- and meso-PSi-Al_2O_3 we can conclude that the former has the higher defected structure originating from the oxygen vacancies. Apparently, the oxygen vacancies increase the adsorption capability of macro-PSi-Al_2O_3. However, the present suggestion is tentative, and requires further theoretical and experimental proof.

4. Conclusions

In this work, ALD Al_2O_3 ultra-thin films grown on macro- and mesoporous silicon surface have been investigated by means of scanning electron microscopy, X-ray photoelectron spectroscopy and energy dispersive X-ray spectroscopy. The chemical composition and morphology of the deposited films and initial porous silicon were established. It was determined that ALD Al_2O_3 layer infiltrates and coats the pores conformally for macro- and mesoporous silicon. Calculated Auger parameter and binding energy analysis confirmed Al_2O_3 formation. Analysis of the inelastic loss spectrum in core-level XPS spectra was used to determine the band gap energies of Al_2O_3. It was suggested that the macro-PSi-Al_2O_3 structures have a high adsorption capability due to oxygen vacancies.

Acknowledgments

Financial support from the National Centre for Research and Development under research grant "Nanomaterials and their application to biomedicine", contract number PBS1/A9/13/2012 is gratefully acknowledged.

References

[1] Garnett EC, Yang P. Silicon nanowire radial p-n junction solar cells. J Am Chem Soc 2008;130:9224–5.
[2] Bettotti P, Pavesi L. Nanosilicon: a new platform for photonics. Phys Status Solidi C 2011;8:2880–4.
[3] Dhanekar S, Jain S. Porous silicon biosensor: current status. Biosens Bioelectron 2013;41:54–64.
[4] Karacali T, Hasar UC, Ozbek IY, Oral EA, Efeoglu H. Novel design of porous silicon based sensor for reliable and feasible chemical gas vapor detection. J Light Technol 2013;31:295–305.
[5] Ge M, Lu Y, Ercius P, Rong J, Fang X, Mecklenburg M, et al. Large-scale fabrication, 3D tomography, and lithium-ion battery application of porous silicon. Nano Lett 2014;14:261–8.
[6] Ge M, Fang X, Rong J, Zhou C. Review of porous silicon preparation and its application for lithium-ion battery anodes. Nanotechnology 2013;24:10.422001.
[7] Aggarwal G, Mishra P, Joshi B, Harsh, Islam SS. Porous silicon surface stability: a comparative study of thermal oxidation techniques. J Porous Mater 2014;21:23–9.
[8] Dingemans G, Kessels WMM. Status and prospects of Al_2O_3-based surface passivation schemes for silicon solar cells. J Vac Sci Technol A 2012;30:040802.
[9] Sarkar S, Culp JH, Whyland JT, Garvan M, Misra V. Encapsulation of organic solar cells with ultrathin barrier layers deposited by ozone-based atomic layer deposition. Org Electron 2010;11:1896–900.
[10] Groner MD, Fabreguette FH, Elam JW, George SM. Low-temperature Al_2O_3 atomic layer deposition. Chem Mater 2004;16:639–45.
[11] Henkel K, Torche M, Sohal R, Karavaev K, Burkov Y, Schwiertz C, et al. Pr-O-Al-N dielectrics for metal insulator semiconductor stacks. Phys Status Solidi A 2011;208:317–29.
[12] Cho M, Park HB, Park J, Hwang CS, Lee JC, Oh SJ, et al. Thermal annealing effects on the structural and electrical properties of HfO_2/Al_2O_3 gate dielectric stacks grown by atomic layer deposition on Si substrates. J Appl Phys 2003;94:2563–71.
[13] Tallarida M, Weisheit M, Kolanek K, Michling M, Engelmann HJ, Schmeißer DJ. Atomic layer deposition of nanolaminate oxide films on Si. Nanopart Res 2011;13:5975–83.
[14] Garces YN, Meyer DJ, Wheeler VD, Liliental-Weber Z, Gaskill DK, Eddy Jr CR. Plasma-assisted atomic layer deposition of nanolaminates for gate dielectric applications. J Vac Sci Technol B 2014;32:03D101.
[15] Wang Wei-Cheng, Lin Che-Wei, Chen Hsin-Jui, Chang Che-Wei, Huang Jhih-Jie, Yang Ming-Jui, et al. Surface passivation of efficient nanotextured black silicon solar cells using thermal atomic layer deposition. ACS Appl Mater Interfaces 2013;5:9752–9.
[16] Bullock J, Yan D, Cuevas A. Passivation of aluminium–n+ silicon contacts for solar cells by ultrathin Al_2O_3 and SiO_2 dielectric layers. Phys Status Solidi RRL 2013:1–4.
[17] Zhao Yan, Zhou Chunlan, Zhang Xiang, Zhang Peng, Dou Yanan, Wang Wenjing, et al. Passivation mechanism of thermal atomic layer deposited Al_2O_3 films on silicon at different annealing temperatures. Nanoscale Res Lett 2013;8:114.

[18] Salem M, Ben Rabha M, Bessais B, Elkhakani MA, Gaidi M. Novel silicon surface passivation by porous silicon combined with an ultrathin Al_2O_3 film. J Mater Sci Mater Electron 2013;24:5035–9.
[19] Ben Rabha M, Salem M, El Khakani MA, Bessais B, Gaidi M. Monocrystalline silicon surface passivation by Al_2O_3/porous silicon combined treatment. Mater Sci Eng B 2013;178:695–7.
[20] Werner F, Cosceev A, Schmidt J. Silicon surface passivation by Al_2O_3: recombination parameters and inversion layer solar cells. Energy Procedia 2012;27:319–24.
[21] Otto M, Kroll M, Käsebier T, Salzer R, Tünnermann A. Extremely low surface recombination velocities in black silicon passivated by atomic layer deposition. Appl Phys Lett 2012;100:191603.
[22] Kemell M, Ritala M, Leskelä M, Groenen R, Lindfors S. Coating of highly porous fiber matrices by atomic layer deposition. Chem Vap Depos 2008;14:347–52.
[23] Lu J, Liu B, Greeley JP, Feng Z, Libera JA, Lei Y, et al. Porous alumina protective coatings on palladium nanoparticles by self-poisoned atomic layer deposition. Chem Mater 2012;24:2047–55.
[24] Elam JW, Libera JA, Pellin MJ. Spatially controlled atomic layer deposition in porous materials. Appl Phys Lett 2007;91:243105.
[25] Huang Z, Geyer N, Werner P, de Boor J, Gösele U. Metal-assisted chemical etching of silicon: a review. Adv Mater 2011;23:285–308.
[26] Mitchell DRG, Triani G, Attard DJ, Finnie KS, Evans PJ, Barbé CJ, et al. Atomic layer deposition of TiO_2 and Al_2O_3 thin films and nanolaminates. Smart Mater Struct 2006;15:S57–64.
[27] Yubero F, Holgado JP, Barranco A, Gonzá lez-Elipe AR. Determination of surface nanostructure from analysis of electron plasmon losses in XPS. Surf Interface Anal 2002;34:201–5.
[28] Moretti G. Auger parameter and Wagner plot in the characterization of chemical states by X-ray photoelectron spectroscopy: a review. J Electron Spectrosc Relat Phenom 1998;95:95–144.
[29] Wagner CD, Passoja DE, Hillery HF, Kinisky TG, Six HA, Jansen WT, et al. Auger and photoelectron line energy relationships in aluminum–oxygen and silicon–oxygen compounds. J Vac Sci Technol 1982;21:933.
[30] Paparazzo E. XPS analysis of iron aluminum oxide systems. Appl Surf Sci 1986;25:1–12.
[31] Sugama T, Carciello N, Taylor C. Pyrogenic polygermanosiloxane coatings for aluminum substrates. J Non-cryst Solids 1991;134:58–70.
[32] Hagio T, Takase A, Umebayashi S. X-ray photoelectron spectroscopic studies of β-sialons. J Mater Sci Lett 1992;11:878–80.
[33] Renault O, Gosset LG, Rouchon D, Ermolieff A. Angle resolved X-ray photoelectron spectroscopy of ultrathin Al_2O_3 films grown by atomic layer deposition. J Vac Sci Technol A 2002;20:1867–76.
[34] Zheng Li, Cheng Xinhong, Cao Duo, Wang Gang, Wang Zhongjian, Xu Dawei, et al. Improvement of Al_2O_3 films on graphene grown by atomic layer deposition with pre-H_2O treatment. ACS Appl Mater Interfaces 2014;6:7014–9.
[35] Jankovsky O, Simek P, Sedmidubsky D, Huber S, Pumera M, Sofer Z. Towards highly electrically conductive and thermally insulating graphene nanocomposites: Al_2O_3–grapheme. RSC Adv 2014;4:7418–24.
[36] Wu Y, Mayer JT, Garfunkel E, Madey TE. X-ray photoelectron spectroscopy study of water adsorption on BaF_2(111) and CaF_2(111) surfaces. Langmuir 1994;10:1482–7.
[37] Haeberle J, Henkel K, Gargouri H, Naumann F, Gruska B, Arens M, et al. Ellipsometry and XPS comparative studies of thermal and plasma enhanced atomic layer deposited Al_2O_3-films. Beilstein J Nanotechnol 2013;4:732–42.
[38] Galuska AA, Uht JC, Marquez N. Reactive and nonreactive ion mixing of Ti films on carbon substrates. J Vac Sci Technol A 1988;6:110.
[39] Nichols MT, Li W, Pei D, Antonelli GA, Lin Q, Banna S, et al. Measurement of bandgap energies in low-k organosilicates. J Appl Phys 2014;115:094105.